Local Mobility in Lipid Domains of Supported Bilayers Characterized by Atomic Force Microscopy and Fluorescence Correlation Spectroscopy

A. R. Burns,* D. J. Frankel,* and T. Buranda†
*Biomolecular Materials and Interfaces Department, MS 1413 Sandia National Laboratories, Albuquerque, New Mexico 87185; and †Department of Pathology, University of New Mexico School of Medicine, Albuquerque, New Mexico

ABSTRACT Fluorescence correlation spectroscopy (FCS) is used to examine mobility of labeled probes at specific sites in supported bilayers consisting of 1,2-dipalmitoyl-*sn*-glycero-3-phosphocholine (DPPC) lipid domains in 1,2-dioleoyl-*sn*-glycero-3-phosphocholine (DOPC). Those sites are mapped beforehand with simultaneous atomic force microscopy and submicron confocal fluorescence imaging, allowing characterization of probe partitioning between gel DPPC and disordered liquid DOPC domains with corresponding topography of domain structure. We thus examine the relative partitioning and mobility in gel and disordered liquid phases for headgroup- and tailgroup-labeled GM1 ganglioside probes and for headgroup- and tailgroup-labeled phospholipid probes. For the GM1 probes, large differences in mobility between fluid and gel domains are observed; whereas unexpected mobility is observed in submicron gel domains for the phospholipid probes. We attribute the latter to domain heterogeneities that could be induced by the probe. Furthermore, fits to the FCS data for the phospholipid probes in the DOPC fluid phase require two components (fast and slow). Although proximity to the glass substrate may be a factor, local distortion of the probe by the fluorophore could also be important. Overall, we observe nonideal aspects of phospholipid probe mobility and partitioning that may not be restricted to supported bilayers.

INTRODUCTION

The lateral organization and dynamics of lipids and proteins in membranes is critical to many cellular processes. Thus there has been considerable interest in the study of membrane microdomains (''lipid rafts'') to determine their size, location, and function in membrane organization (1–3). Studies of domains in cellular membranes have relied heavily on fluorescence-based imaging of protein colocalization and lipid structure (4–6) and fluorescence-based dynamical studies of lipid probes and labeled proteins. Concerning dynamics, it is widely held that translational diffusion rates reflect not only the intrinsic mobility of membrane constituents but also the local structure of the membrane. Thus we have seen the application of a variety of techniques that offer considerable insight into diffusion processes in cellular membranes at various length scales. These include fluorescence recovery after photobleaching (FRAP) (7,8), single particle tracking (SPT) (7,9,10), and fluorescence correlation spectroscopy (FCS). Applications of FCS to diffusion in membranes have been discussed comprehensively in the literature (11–15). Since the sensitivity of time-dependent statistical analysis of fluorescence intensity in FCS scales inversely with detection volume and probe concentration, it is an excellent tool to complement low-light-level confocal fluorescence imaging of membranes.

Both fluorescence-based imaging and dynamics have also been essential to the analysis of the structure of lipid domains and component mobility in model membranes. Model membrane studies offer the ability to characterize phase separation, due to headgroup interactions and/or acyl chain structure, of gel or liquid-ordered domains (''rafts'') within multicomponent lipid mixtures, on the basis of subsequent partitioning of lipid probes or protein-binding glycosphingolipids between the phases (16–19). By partitioning, we refer to the process by which probes go preferentially into one domain but can be observed in both. It has been shown using FCS (20,21), FRAP (22,23), and SPT (24,25) that the two-dimensional lateral diffusion coefficient of most probes is strongly dependent on the lipid packing of the domains: $\sim$1–10 $\times$ 10^{-8} cm^2/s in liquid-disordered phases to essentially immobile ($<10^{-11}$ cm^2/s) in gel phases.

Since dynamical processes are dependent on the local membrane structure as well as local molecular interactions, it would be advantageous to directly correlate dynamics information with detailed lateral dimensions and topography mapped out with atomic force microscopy (AFM). AFM has been successfully used to image domain structure in supported lipid monolayers and bilayers in fluid environments on the basis of topographic height differences between gel-phase, liquid-ordered, and liquid-disordered domains (23,26–28). Recently, simultaneous AFM and confocal fluorescence imaging was used to examine the partitioning of lipid probes between fluid and gel domain boundaries mapped with 1 nm lateral resolution (28). We now present FCS measurements of diffusion coefficients of lipid and glycolipid probes at precisely defined locations on supported bilayers mapped out with the same technique. The resolution is limited only by the spot size ($\sim$400 nm) of the laser beam on the sample. Of particular interest is the boundary region between domains. Also, it has been shown that the location of the fluorescent probe (e.g., headgroup versus tailgroup) on the lipid molecule has significant impact on partitioning between domains (18,19,28). Since partitioning and lateral diffusion are both

Submitted January 28, 2005, and accepted for publication April 29, 2005.
Address reprint requests to Alan R. Burns, E-Mail: aburns@sandia.gov.

0006-3495/05/08/1081/13 $2.00
doi: 10.1529/biophysj.105.060327

expected to be sensitive to local molecular interactions, it is of interest to determine if the location of the fluorescent probe influences the lateral diffusion as well. Thus, we examine the relative partitioning and diffusion coefficients in gel (DPPC) and disordered liquid (DOPC) phases and boundary regions for both headgroup- and tailgroup-labeled GM1 ganglioside as well as for headgroup- and tailgroup-labeled phospholipid analogs of DPPC. Since GM1 selectively binds cholera toxin B (CTX-B) fragments, we are also able to examine the effects of protein binding on GM1 mobility in the fluid DOPC phase.

Numerous studies of supported bilayers in fluid environments have shown that domain structure and freedom of movement of lipid components are, for the most part, preserved relative to unsupported membranes (22,23,29–32). This behavior is attributed to a 1–2 nm water layer that decouples the bilayer from the solid support and allows ''lateral'' lipid-lipid and ''vertical'' leaflet-leaflet interactions to dominate (33–35). Substrate effects have been reported, however, and include slower diffusion rates for probes proximal to the substrate (36) and altered phase behavior (37,38). The latter may be due to unrelieved stresses at domain boundaries created during bilayer formation and/or temperature cycling (39). Our results do indicate local heterogeneities in gel domain structure and a slow mobility component in the phospholipid probes. However, it is not clear whether those can be attributed to substrate effects or defects induced by the probes.

MATERIALS AND METHODS

Lipids and proteins

1,2-dipalmitoyl-*sn*-glycero-3-phosphocholine (DPPC), 1,2-dioleoyl-*sn*-glycero-3-phosphocholine (DOPC), and GM1 ovine brain ganglioside (GM1) were purchased from Avanti Polar Lipids (Alabaster, AL) and used without further purification. *N*-(4,4-difluoro-5,7-dimethyl-4-bora-3a,4a-diaza-s-indacene-3-propionyl)-1,2-dipalmitoyl-*sn*-glycero-3-phosphoethanolamine (BODIPY-DPPE, also known as BODIPY-DHPE), 2-(4,4-difluoro-5,7-dimethyl-4-bora-3a,4a-diaza-s-indacene-3-dodecanoyl)-1-hexadecanoyl-*sn*-glycero-3-phosphocholine (BODIPY-C12-DHPC), *N*-(4,4-difluoro-5,7-dimethyl-4-bora-3a,4a-diaza-s-indacene-3-propionyl)-C5-ganglioside GM1 (BODIPY-C5-GM1), biotinylated recombinant CTX-B subunit (B-CTX-B), Alexa Fluor 488 conjugated recombinant CTX-B subunit (Alexa-488 CTX-B), and Alexa Fluor 488 hydrazide were purchased from Molecular Probes (Eugene, OR) and used without purification unless otherwise indicated. Sodium meta-periodate and bovine brain asialoganglioside-GM1 were purchased from Sigma Chemical (St. Louis, MO) and used without further purification. It should be noted that the use of recombinant Alexa Fluor 488 CTX-B greatly reduces background emission that is found when non-recombinant CTX-B is used (28).

Synthesis of headgroup-labeled GM1 ganglioside

Alexa Fluor 488 hydrazide-conjugated GM1 (''Alexa-488 head-GM1'') was prepared by a modification of previous methods (40). Bovine brain asialoganglioside-GM1 (1 mg/mL) was suspended in 100 mM sodium acetate buffer (pH 5.5) with 1 mM sodium meta-periodate. The oxidation reaction was allowed to proceed for 30 min on ice. The suspension was then purified and concentrated by ultrafiltration in the same buffer using YM-30 Microcon centrifugal filters (Millipore, Bedford, MA), repeating five times to remove the sodium-meta periodate. A total of 10 mM Alexa Fluor 488 hydrazide was added to the oxidized GM1 and allowed to react with agitation for 2 h at room temperature. The fluorescent GM1 conjugates were freed of unreacted dye by using YM-30 Microcon centrifugal filters, repeating in PBS buffer, as described above, until the supernatant was optically clear. The labeled GM1 was dried under vacuum and stored as a powder under nitrogen at −20°C. Based on the mass of the GM1 before and after dye conjugation and absorption measurements, the Alexa:GM1 ratio was determined to be unity.

Supported bilayers

Lipid bilayers are formed on glass coverslips by the method of vesicle fusion (29,35). Small unilamellar vesicles are prepared by first dissolving the lipids in chloroform (Alexa-488 head-GM1 was dissolved in dimethyl sulfoxide), followed by rotary evaporation of the solvent and drying for over 12 h under high vacuum. The lipids are resuspended by adding phosphate-buffered saline (PBS) buffer (100 mM NaCl, 40 mM sodium phosphate, pH 7.4) and vortexing, followed by degassing with nitrogen. The lipid suspension was then subjected to a freeze thaw cycle followed by repeated extrusion (Northern Lipids, Vancouver, Canada) through 100 nm filter pores. Dynamic light scattering characterization (Protein Solutions, High Wycomb, UK) verified 100 nm vesicle diameters.

Glass coverslips (0.13–0.17 mm thickness) are cleaned in (7:3) H_2SO_4/H_2O_2 (caution: this is potentially explosive when reacting with organics), rinsed thoroughly in distilled water and ultrapure water (Barnstead Nanopure, Dubuque, IA), and stored under ultrapure water (18 MΩ-cm). Just before use, the coverslips are dried under a stream of pure, dry nitrogen and mounted in a Leiden coverslip dish (Harvard Apparatus, Holliston, MA). The ~3 mM vesicle solution is pipetted onto the coverslip and diluted (1:5) with imaging PBS buffer (150 mM NaCl, 50 mM sodium phosphate, 1. 5 mM NaN_3, pH 7.4). After 2 h of incubation at 60°C followed by 30 min of cooling to room temperature, the lipid bilayer is rinsed thoroughly with imaging PBS buffer and mounted on the microscope. When required, incubation of the lipid bilayers with Alexa 488-CTX-B or B-CTX-B stock solutions (10 μgr/ml, in imaging PBS buffer) is performed for 1–2 min, followed by thorough rinsing with imaging PBS buffer.

AFM and fluorescence microscopy

The experimental apparatus for obtaining simultaneous AFM and fluorescence images of lipid bilayers has been described previously and will be summarized here (28). An inverted microscope was modified to accommodate an AFM scan head and is mounted on an acoustically and light-baffled vibration isolation air table. The liquid cell (coverslip dish) is mounted on a flat-plate, closed-loop XY scanner (Mad City Labs, Madison, WI). Excitation light from a continuous 488 nm Ar^+ laser on a separate table is coupled into a single-mode optical fiber that forms a collimated Gaussian output beam. The beam reflects off a dichroic mirror and underfills (~80%) the back plane of a 100× (1.3 NA) oil immersion objective. The latter is used to optimize two-dimensional imaging and FCS work at the flat interface of the supported bilayer and the glass coverslip (41). The objective focuses the light (300 nW) to a diffraction-limited ~400 nm spot (see below) spatially coincident on the sample with the pyramidal tip on the end of the AFM cantilever, as can been seen through the microscope eyepiece. This alignment remains fixed as the sample is scanned. The optical resolution of the fluorescence image is optimized by minimizing the spot size on the sample. Epifluorescence emission passes through two notch filters (488 and 670 nm) and a 500–580 nm band-pass filter and is then spatially filtered by a 50-μm diameter core multimode fiber connected to an avalanche photodiode detector. Before a scan, the fluorescence signal from the minimized laser spot is optimized by the lateral and translational position of this 50-μm aperture.

Simultaneous AFM topographic and fluorescence images are acquired by a single controller for sample scanning, AFM feedback, and photon counting of the fluorescence. Closed-loop control of the XY scanner is performed automatically by separate electronics that are interfaced to the imaging controller. The XY scanner plate was calibrated with a 463 nm square grid grating (Ted Pella, Redding, CA), and the AFM head was calibrated in Z with known 25.5 nm steps (TGZ01, NT-MDT, Mikromasch USA, Portland, OR). Fluorescence background count rates for blank substrates were <1 KHz. A slight offset between the two images is possible due to the manual alignment of the laser focus on the AFM probe tip. All the AFM data presented here were acquired with cantilevers (Olympus TR400-PSA, Tokyo, Japan, nominal force constant of 0.08 N/M) in tapping mode.

Fluorescence correlation spectroscopy

FCS was performed with the AFM-fluorescence imaging apparatus discussed above in conjugation with a correlator (ALV-6010/160, Langen, Germany) interfaced to a separate computer using software supplied with the correlator (ALV Correlator Software Version V.3.1.12). Calibration of the laser spot size ($1/e^2$ Gaussian radius $= 0.22$ μm for 488 nm light) on the surface of the coverslip at the same power level (300 nW) and same optical pathway used for all imaging and FCS was determined by fitting the diffusion data acquired for a 10^{-7} M solution of rhodamine 6G in a coverslip dish to the value 2.8×10^{-6} cm^2/s (42). Precise control of the laser spot position on the sample was maintained by the closed-loop XY scanner, which eliminates drift and nonlinearities common to piezoceramic actuators used in AFM (43). The laser spot focus and the 50-μm multimode fiber spatial filter are optimized as discussed above for imaging. FCS data acquisition was performed as follows: 1), 256×256 pixel AFM and fluorescence images of supported bilayers were acquired and stored in memory; 2), the AFM cantilever was withdrawn from the sample to minimize light scattering (a precaution, not a problem); 3), the APD signal output was disconnected from the fluorescence imaging photon counter and connected directly to the correlator with an impedance-matched cable; 4), the fluorescence image was displayed and, with an image controller cursor, the position of the XY scanner was moved to a spot in the fluorescence image; and 5), FCS data was acquired for 100 seconds at that spot. The correlator also monitored the fluorescence count rate so that photobleaching could be detected if occurring. Steps 4 and 5 were repeated for many different spots in the fluorescence image. The raw FCS data were not averaged at one spot, but rather many spots were sampled and analyzed independently. Diffusion coefficients were then averaged, unless otherwise noted.

Analysis of FCS data for two-dimensional translational diffusion has been thoroughly discussed elsewhere (11–13) and will be briefly summarized here. Fluctuations $\delta F(t) = F(t) - \langle F(t)\rangle$ in the fluorescence intensity F are autocorrelated over discrete time intervals τ by the function $G(\tau)$:

$$G(\tau) = \langle \delta F(t)\delta F(t+\tau)\rangle / \langle F\rangle^2. \quad (1)$$

Brownian diffusion has a mean square displacement $\langle x^2\rangle = 4D\tau$, where D is the sought after diffusion coefficient. It can be shown that for fluorescence fluctuations due to two-dimensional diffusion of N molecules (11)

$$G(\tau) = \frac{1}{N}\sum_{\mathrm{j}} \frac{Cj}{(1+\tau/\tau_{\mathrm{d,j}})}, \quad (2)$$

where $\tau_{\mathrm{d,j}} = w^2/4D_{\mathrm{j}}$ is the average residence interval for molecular component j with fraction C_{j} within the confines of the Gaussian beam waist w. Other factors that may contribute to fluorescence fluctuations, such as single-triplet intersystem crossing (44), were found to be negligible for the dyes and timescales used in these experiments. For labeled probe molecules of one type undergoing unrestricted lateral diffusion, Eq. 2 reduces to a single component (D) fit. However, if sample heterogeneities exist, the data may exhibit two components, ''fast'' and ''slow'', with fractions C_{fast} and C_{slow} and diffusion coefficients D_{fast} and D_{slow}, respectively.

RESULTS AND DISCUSSION

Simultaneous AFM-fluorescence imaging of probe partitioning

In this section, we present simultaneous AFM-fluorescence images of bilayers (all 3:1 DOPC/DPPC) having various headgroup- and tailgroup-labeled GM1 and phospholipid analog fluorescent probes. The images are acquired under the same optical conditions that are subsequently used for the FCS experiments. Thus they not only provide information with regard to domain structure and probe partitioning but also serve as ''maps'' to guide the location of the FCS data acquisition. The probe concentrations are $\sim$0.05% so that both imaging and FCS can be performed on the same sample in sequence. These low probe concentrations preclude precise quantitative partitioning analysis; thus only qualitative characterization is presented.

Since, as we discuss below, the presence of fluorophores can change the partitioning of lipids between liquid-disordered and gel domains, we begin by discussing simultaneous AFM-fluorescence images of bilayers that contain 0.5% unmodified GM1 that partitions strongly into the tightly packed DPPC gel domains (17,45). (We used 0.5% GM1 rather than 0.05% to make certain that a detectable amount is in the DOPC fluid phase for FCS discussed below.) In Fig. 1 *A*, it can be seen from the AFM topography that the DPPC forms (bright) irregularly shaped gel domains. The DPPC-DOPC height difference is 1.1 ± 0.2 nm, in agreement with other studies (26,46). When the unlabeled GM1 is stained by bound Alexa-488 CTX-B (17,45), the DPPC domains become 3.5 ± 0.2 nm higher that the DOPC fluid phase, in agreement with neutron reflectivity measurements (47). The Alexa-488 CTX-B is closely packed and uniformly covers the gel domains, indicating significant GM1 concentration. The GM1 preference for the gel domains is also clearly verified in the fluorescence image (Fig. 1 *B*), where the bright domains correlate with the AFM topography. The resolution

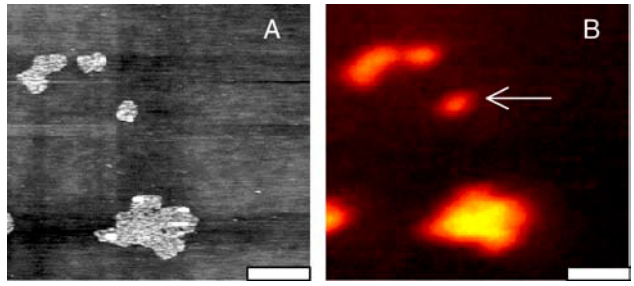

FIGURE 1 Simultaneous 5 μm AFM topography (*A*) and fluorescence (*B*) images (scale bar $= 1$ μm) of a 3:1 DOPC/DPPC with 0.5% GM1 bilayer on glass. The GM1 partitions to the DPPC domains where it binds Alexa-488 CTX-B. In the topography image, the bright DPPC domains usually are 1.1 ± 0.2 nm higher than the surrounding DOPC; in this case, having bound Alexa-488 CTX-B, they are 3.5 ± 0.2 nm higher. The fluorescence feature indicated by the arrow in *B* is resolved with a full width at half-maximum of $\sim$300 nm.

of the smallest domains in the fluorescence image is at the diffraction limit (~300 nm full width half height), consistent with the FCS Gaussian beam waist calibration discussed in the previous section.

The partitioning in the 3:1 DOPC/DPPC domain structure of three probes used in this study differs considerably from that of unlabeled GM1. From the images shown in Fig. 2, one can see that the dark regions of the fluorescence images (indicating exclusion of the probe) correlate with the DPPC gel domains in the topography images (bright areas 1.1 ± 0.2 nm higher than DOPC). Thus the ''tailgroup-labeled GM1'' (BODIPY-C5-GM1) in Fig. 2, *A* and *B*, the ''tailgroup-labeled phospholipid'' (BODIPY-C12-DHPC) in Fig. 2, *E* and *F*, and the ''headgroup-labeled phospholipid'' (BODIPY-DHPE) in Fig. 2, *G* and *H*, are all excluded in varying degrees from the DPPC gel domains. The same probes, as well as similar probes using different fluorophores, have exhibited exclusion from ordered domains in other supported and unsupported monolayers (16,17,45,48) as well as bilayer vesicles (20,49). The presence of the fluorophore on saturated

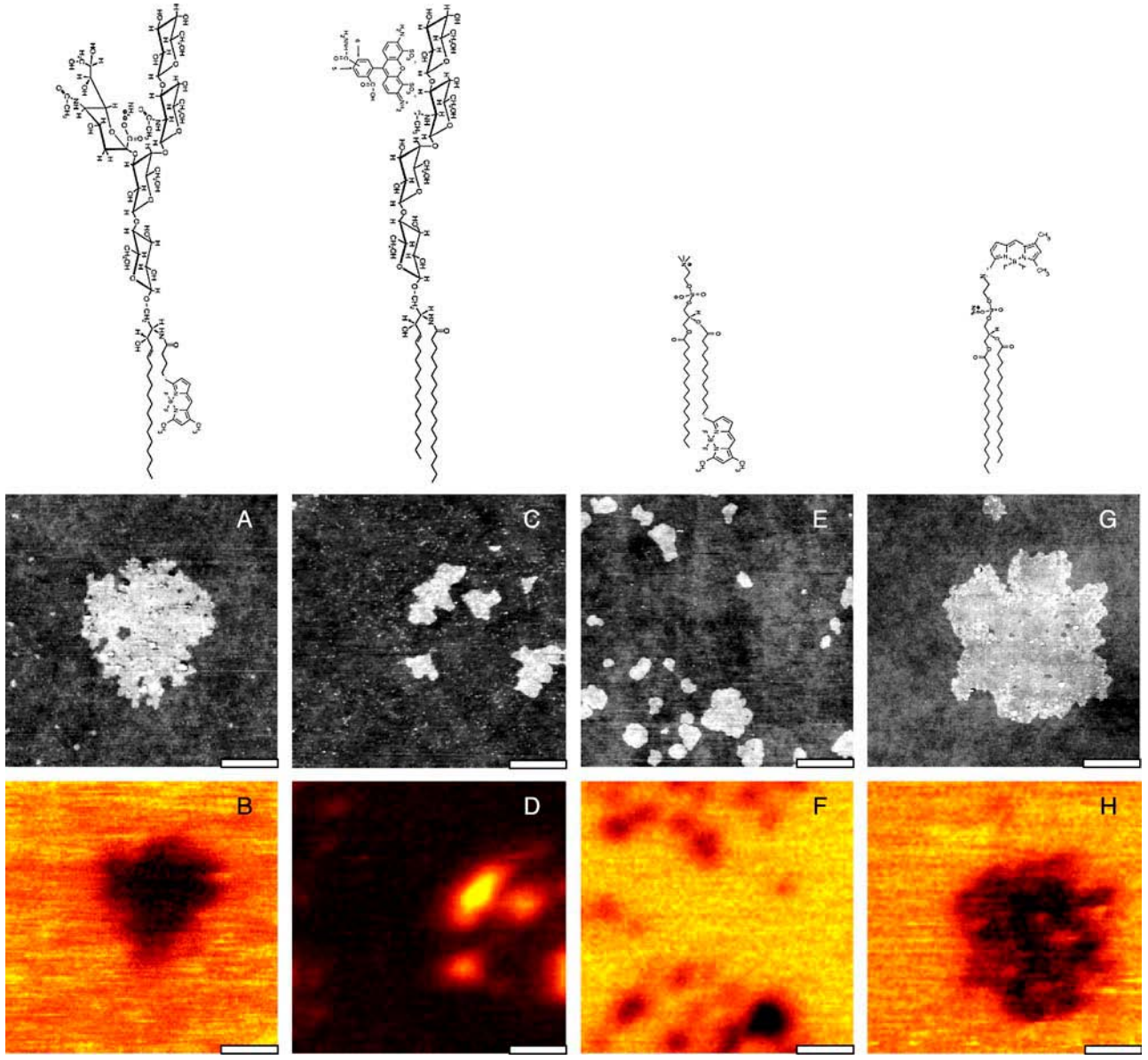

FIGURE 2 Simultaneous AFM topography (*middle row*) and fluorescence (*bottom row*) imaging of 3:1 DOPC/DPPC bilayers on glass with four different lipid probes. All images are 5 μm scans (scale bar = 1 μm). In the AFM images, the bright DPPC domains are 1.1 ± 0.2 nm higher than the surrounding DOPC. In the fluorescence images, the dark regions (less intensity) indicate exclusion of the probe lipids. In *A* and *B*, the probe is 0.05% BODIPY-C5-GM1. In *C* and *D*, the probe is 0.03% Alexa-488 head-GM1. In *E* and *F*, the probe is 0.05% BODIPY-C12-DHPC. In *G* and *H*, the probe is 0.05% BODIPY-DHPE. Structures of the probes (*top row*, above corresponding AFM and fluorescence images) are illustrative and meant for relative comparison. For the Alexa-488 head GM1, it is not known which sugar group binds the Alexa-488 hydrazide.

tailgroups thus sufficiently perturbs the local packing of the lipid chains to be excluded from the ordered DPPC domains (19). This is expected for the short chain position of the BODIPY-C5-GM1. However, even the long-chain position of BODIPY-C12-DHPC does not improve its accommodation in the DPPC. Even more surprising, perhaps, is the exclusion of the BODIPY-DHPE, since the unaltered saturated acyl chains match DPPC. The exclusion from DPPC gel domains of other headgroup-labeled lipids derived from DPPE have also been reported for unsupported monolayers and bilayers (45,50). It should be pointed out, however, that partitioning is not solely driven by lipid phase. For example, in DLPC/DPPC mixtures with coexisting phases, *N*-rhodamine-DHPE was found to favor the DPPC gel phase (51). This is most likely due to more favorable hydrophobic matching.

The one exception to exclusion from DPPC seen in Fig. 2 is the preference for DPPC domains of Alexa-488 head-GM1 (Fig. 2, *C* and *D*). It is thus very significant that the large GM1 headgroup, even when conjugated with Alexa-488, is accommodated in the densely packed, ordered DPPC domains. Since all the partitioning results depicted in Fig. 2 have been observed in unsupported bilayers as well, we can conclude that probe partitioning in these supported bilayers does not appear to be qualitatively influenced by substrate interactions but rather by interactions in the bilayer.

The irregular shapes of the DPPC gel domains have also been observed in unsupported vesicles (20,49,52). The large domains in Fig. 2 are most likely formed by diffusion-limited Ostwald ripening at the expense of smaller domains during cooling of the sample to room temperature (53). However, apparent pockets of trapped DOPC and fluorescent probes in some DPPC domains (e.g., Fig. 2 *H*) suggest that aggregation also occurs to some extent during the cooling period. All features in the AFM images are static at room temperature. There are some very small (<50 nm) gel domains present as well. These small domains are well below the optical resolution in the fluorescence images and thus would never be seen in a fluorescence-only study. Finally, another observation reported in vesicle studies (20,49) is the symmetrical distribution of lipid domains across the bilayer, indicating strong coupling of the two monolayer leaflets. Evidence for similar behavior here can be found in the consistent correlation of domains in the topographic images with all features in the fluorescence images; e.g., there has been no observation in the fluorescence images of domains in the lower leaflet (proximal to the substrate) that do not have a corresponding topographic domain in the upper (distal) leaflet.

Site dependence of local mobility

In this section, we discuss the results of site-specific FCS measurements that relate to structural features in the AFM/fluorescence images, specifically DPPC domains and DOPC/DPPC domain boundaries. Since FCS can be readily performed at low probe concentrations (11), there is sufficient sensitivity for data acquisition in the dark regions of the fluorescence images. For the sake of clarity, we show only the fits to the FCS data in Figs. 4–7; representative FCS data can be seen in Figs. 8 and 9. With respect to domain boundaries, it is of particular interest to see if mobility in the DOPC phase is influenced by the proximity of ordered DPPC domains due to extended ordering (30) or to strains associated with boundary line tensions and/or gel domain formation (39). There are two important aspects of data acquisition that are imposed by the diffraction-limited optical resolution. These are illustrated in Fig. 3, where we have superimposed the DPPC domain boundaries, as determined from AFM, on the corresponding fluorescence image. Also depicted is the approximate FCS spot size (~400 nm) relative to the domain features. The first aspect to note is that the domain boundaries will always be blurred in the fluorescence images relative to the AFM topography. One can see in Fig. 3 that the true (AFM) boundaries are in the ''gray'' or intermediate intensity region of the fluorescence images. Since there can be an offset between the AFM and fluorescence images, we must use the fluorescence image to position the FCS spot. Thus we rely on these gray regions to select domain boundaries. Although the spot selection may be somewhat imprecise relative to the AFM image, the stability of the location is maintained by the closed-loop scanner. The second aspect to point out is that the smaller domains (<500 nm) tend to have diminished contrast in the fluorescence image. Since they stand out nicely in the AFM image, we can refer to the AFM data to verify that they are indeed domains.

In Fig. 4, we show very large differences in the mobility of Alexa-488 head-GM1 depending on the location of the

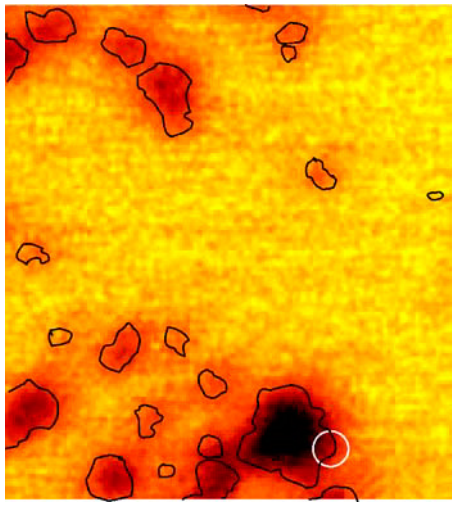

FIGURE 3 Overlap of simultaneous AFM and fluorescence images of 0.05% BODIPY-C12-DHPC taken from Fig. 2, *E* and *F*. For clarity, the AFM topographic image (Fig. 2 *E*) was processed in Adobe Photoshop (San Jose, CA) to display just the line edges of the DPPC domains. The white circle (used also as scale marker) is the approximate size of the calibrated FCS spot (400 nm diameter). It is located at a domain boundary that appears ''gray'' (intermediate intensity) in the fluorescence image.

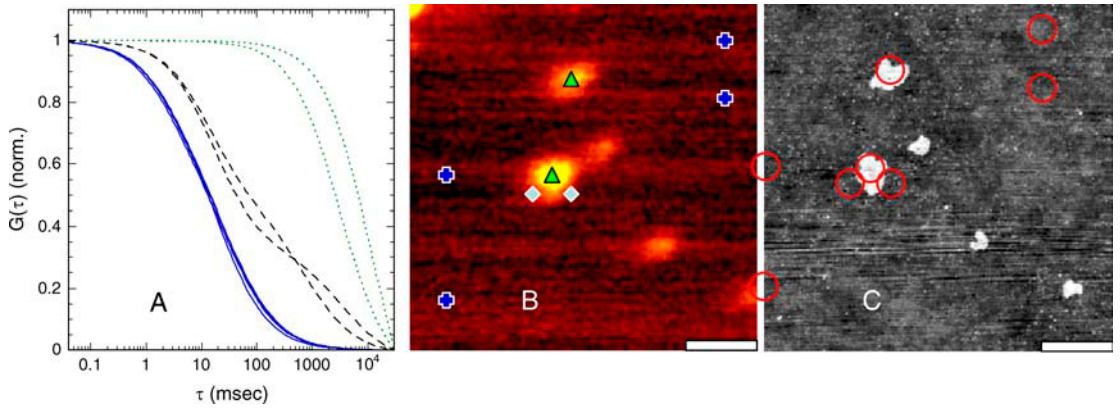

FIGURE 4 Representative FCS measurements in regions of supported bilayer of 3:1 DOPC/DPPC with 0.03% Alexa-488 head-GM1. (*A*) Fits to normalized autocorrelation curves (data curves not shown for clarity) acquired at specific sites indicated in fluorescence image (*B*). Diffusion coefficients are discussed in text. The solid curves are for DOPC regions marked by crosses, the dashed curves are for DOPC/DPPC boundary regions marked by diamonds, and the dotted curves are for DPPC domains marked by triangles. (*B*) Fluorescence image of Alexa-488 head-GM1, where bright regions are DPPC gel domains. (*C*) AFM topography acquired simultaneously with fluorescence image. Bright features are DPPC domains 1.1 ± 0.2 nm higher than the surrounding DOPC. The circles are the approximate size of the calibrated FCS spot and correspond to the locations selected in the fluorescence image. Images (*B* and *C*) are 5 μm scans (scale bar = 1 μm).

FCS measurement in the bilayer. The mobility in the DOPC region (*crosses* in Fig. 4 *B*, *solid curves* in Fig. 4 *A*) is consistently rapid ($D > 10^{-8}$ cm^2/s) and independent of location. Meanwhile, representative data for FCS locations inside the DPPC gel domains (*triangles* in Fig. 4 *B*, *dotted curves* in Fig. 4 *A*) reflect immobility ($D < 10^{-11}$ cm^2/s), which is verified by significant photobleaching. Similar FCS results were reported for DOPC/DPPC mixed vesicles (21). Thus the dense packing of the gel domains accommodates the Alexa-488 head-GM1, given the bright fluorescence in these regions, but also completely prevents mobility. For those points selected along the boundaries, the FCS data is characterized by distinct two-component fits reflecting the heterogeneity of the lipid packing at the domain boundary. Examples are shown in Fig. 4 (*diamonds* in Fig. 4 *B*, *dashed curves* in Fig. 4 *A*). The D_{fast} components of the two-component curve fits shown here range from 7–9 $\times$ 10^{-9} cm^2/s, the D_{slow} components range from 0.3–1.4 $\times$ 10^{-10} cm^2/s, and C_{fast}/C_{slow} ranges from 1–2. The multiple diffusion coefficients suggest a contribution from both fluid DOPC and gel DPPC phases, although according to the AFM map these FCS spots were predominately in the DOPC phase. We do not see evidence of a smooth transition in mobility between the two phases, and it is possible that the

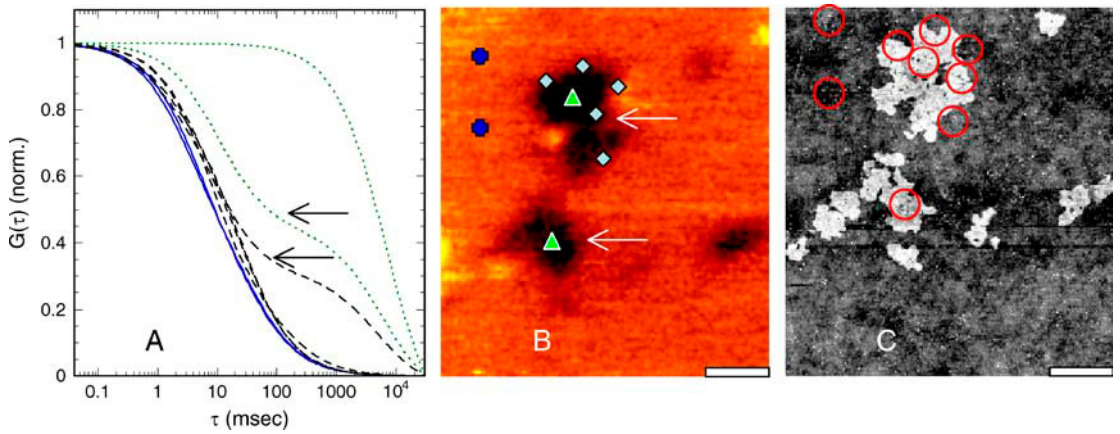

FIGURE 5 Representative FCS measurements in regions of supported bilayer of 3:1 DOPC/DPPC with 0.05% BODIPY-C5-GM1. (*A*) Fits to normalized autocorrelation curves (data curves not shown for clarity) acquired at specific sites indicated in fluorescence image (*B*). Diffusion coefficients are discussed in text. The solid curves are for DOPC regions marked by crosses, the dashed curves are for DOPC/DPPC boundary regions marked by diamonds, and the dotted curves are for DPPC domains marked by triangles. The selected dashed curve (*arrow*) corresponds to data acquired at diamond indicated by arrow in (*B*). The selected dotted curve (*arrow*) corresponds to data acquired at triangle indicated by arrow in (*B*). (*B*) Fluorescence image of BODIPY-C5-GM1, where dark regions represent exclusion from DPPC gel domains. (*C*) AFM topography acquired simultaneously with fluorescence image. Bright features are DPPC domains 1.1 ± 0.2 nm higher than the surrounding DOPC. The circles are the approximate size of the calibrated FCS spot and correspond to the locations selected in the fluorescence image. Images (*B*,*C*) are 5 μm scans (scale bar = 1 μm).

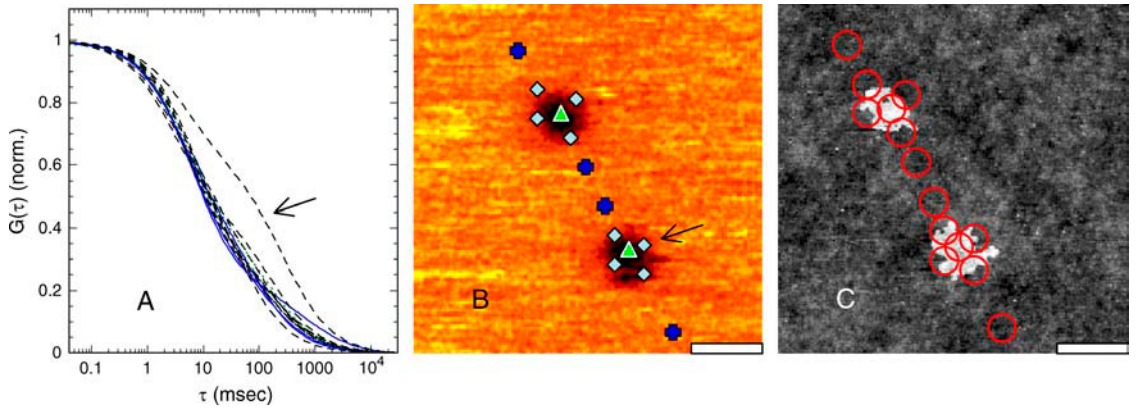

FIGURE 6 Representative FCS measurements in regions of supported bilayer of 3:1 DOPC/DPPC with ~0.05% BODIPY-DHPE. (*A*) Fits to normalized autocorrelation curves (data curves not shown for clarity) acquired at specific sites indicated in fluorescence image (*B*). Diffusion coefficients are discussed in text. The solid curves are for DOPC regions marked by crosses, the dashed curves are for DOPC/DPPC boundary regions marked by diamonds, and the dotted curves are for DPPC domains marked by triangles. The selected dashed curve (*arrow*) corresponds to data acquired at diamond indicated by arrow in *B*. (*B*) Fluorescence image of BODIPY-DHPE, where dark regions represent exclusion from DPPC gel domains. (*C*) AFM topography acquired simultaneously with fluorescence image. Bright features are DPPC domains 1.1 ± 0.2 nm higher than the surrounding DOPC. The circles are the approximate size of the calibrated FCS spot and correspond to the locations selected in the fluorescence image. Images (*A* and *B*) are 5 μm scans (scale bar = 1 μm).

nearby DPPC gel domain is influencing the Alexa-488 head-GM1 mobility in the DOPC phase.

In the case of BODIPY-C5-GM1, many probes along the domain boundaries appeared to be fully mobile. Representative data are shown in Fig. 5 where one can see that there is little difference in the mobility of those lipids along the domain boundary (*diamonds* in Fig. 5 *B*, *dashed curves* in Fig. 5 *A*) with those in the DOPC phase (*crosses* in Fig. 5 *B*, *solid curves* in Fig. 5 *A*). One exception (*diamond* indicated by *arrow* in Fig. 5 *B*) has a distinct two-component fit that most likely reflects a significant immobile fraction from the DPPC domain ($D_{fast} \approx 2 \times 10^{-8}$ cm^2/s, $D_{slow} \approx 3 \times 10^{-11}$ cm^2/s, and $C_{fast}/C_{slow} \approx 2$). Inside the larger DPPC domains (>1 μm), the BODIPY-C5-GM1 probes are immobile. However, we have detected instances (*highlighted triangle* in Fig. 5 *B*, *dotted curves* in Fig. 5 *A*) of significant mobility inside smaller domains. The corresponding autocorrelation curve is another distinct two-component fit, with $D_{fast} \approx 1 \times 10^{-8}$ cm^2/s, $D_{slow} \approx 2 \times 10^{-11}$ cm^2/s, and $C_{fast}/C_{slow} \approx 1.1$. Thus it appears that we have detected heterogeneities in DPPC gel domains.

We saw in Figs. 4 and 5 that the GM1 probes, particularly Alexa-488 head-GM1, exhibit the expected large changes in mobility when the FCS interrogation spot is moved from DOPC to DPPC domains. Alexa-488 head-GM1 probes are immobile in the smallest DPPC domains (<1 μm) that still fully contained the FCS spot without overlapping the boundary, whereas the BODIPY-C5-GM1 does exhibit limited mobility in some submicron DPPC domains. In stark contrast, however, we unexpectedly find that the

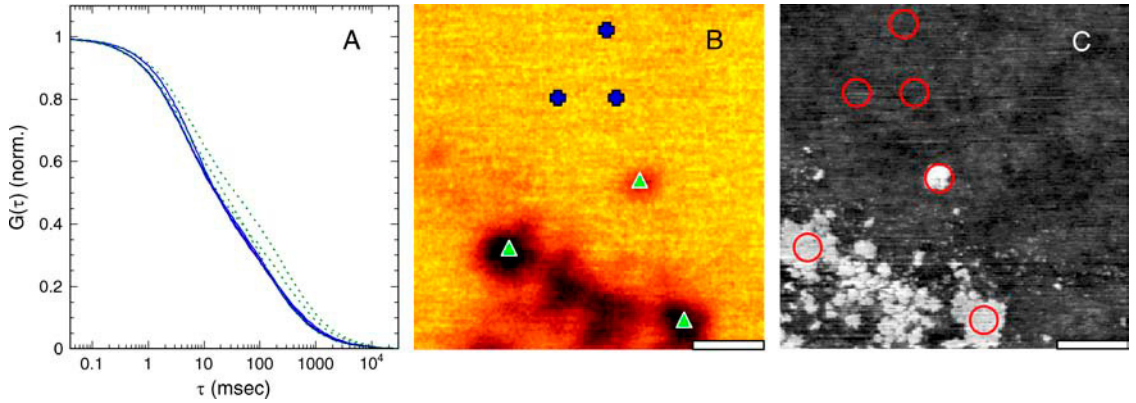

FIGURE 7 Representative FCS measurements in regions of supported bilayer of 3:1 DOPC/DPPC with ~0.05% BODIPY-C12-DHPC. (*A*) Fits to normalized autocorrelation curves (data curves not shown for clarity) acquired at specific sites indicated in fluorescence image (*B*). Diffusion coefficients are discussed in text. The solid curves are for DOPC regions marked by crosses, and the dotted curves are for DPPC domains marked by triangles. (*B*) Fluorescence image of BODIPY-C12-DHPC, where dark regions represent exclusion from DPPC gel domains. (*C*) AFM topography acquired simultaneously with fluorescence image. Bright features are DPPC domains 1.1 ± 0.2 nm higher than the surrounding DOPC. The circles are the approximate size of the calibrated FCS spot and correspond to the locations selected in the fluorescence image. Images (*A* and *B*) are 5 μm scans (scale bar = 1 μm).

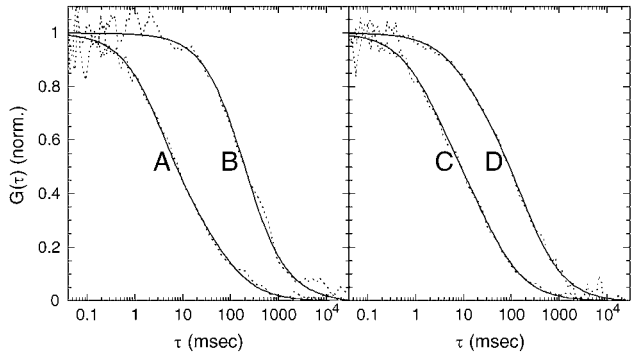

FIGURE 8 Effects of CTX-B binding on lateral diffusion of GM1 in DOPC regions of 3:1 DOPC/DPPC bilayers. Typical normalized autocorrelation curves of (*A*) 0.03% Alexa-488 head-GM1; (*B*) trace amounts of GM1 in DOPC bound to Alexa-488-CTX-B; (*C*) 0.05% BODIPY-C5-GM1; and (*D*) 0.05% BODIPY-C5-GM1 bound to B-CTX-B. The solid curves are fits to the data (*dotted curves*). Diffusion coefficients are discussed in text and summarized in Table 1.

mobility of the BODIPY-DHPE and BODIPY-C12-DHPC probes in DPPC domains of similar submicron size is almost indistinguishable from that in the fluid DOPC. An example of the surprising results is shown in Fig. 6, where a series of FCS curves were acquired for BODIPY-DHPE at indicated locations in and around DPPC domains that are ~0.5 μm in size. The mobility inside these DPPC domains (*triangles* in Fig. 6 *B*, *dotted curves* in Fig. 6 *A*) is almost the same as that

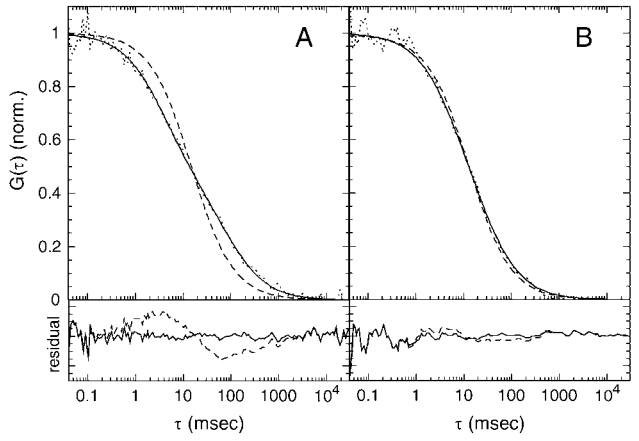

FIGURE 9 One-component versus two-component fits to normalized autocorrelation curves for lateral diffusion in DOPC. (*A*) Typical curve fits to BODIPY-DHPE and BODIPY-C12-DHPC autocorrelation curves (in this case, BODIPY-DHPE), where the dotted curve is the normalized autocorrelation data, the solid curve is the best two-component fit, and the dashed curve is the best one-component fit. It is clear from the curves and the residuals (*below*) that a two-component fit is required. (*B*) Typical curve fits to unbound Alexa-488 head-GM1 and BODIPY-C5-GM1 autocorrelation curves (in this case, Alexa-488 head-GM1), where the dotted curve is the normalized autocorrelation data, the solid curve is the best two-component fit, and the dashed curve is the best one-component fit. The residuals indicate a close fit for the one-component model, but the two-component model is slightly better. Diffusion coefficients are discussed in text and summarized in Table 1.

in the DOPC regions (*crosses* in Fig. 6 *B*, *solid curves* in Fig. 6 *A*). The only curve that has a significant slow component (indicated by *arrow*) was acquired on a domain boundary ($D_{fast} \approx 3 \times 10^{-8}$ cm^2/s, $D_{slow} \approx 4 \times 10^{-10}$ cm^2/s, $C_{fast}/C_{slow} \approx 0.7$). Similar behavior is observed for BODIPY-C12-DHPC in ~700 nm domains (Fig. 7). We found immobility only at the center of large DPPC domains (>1 μm) where the fluorescence intensity is at a minimum (not shown).

The apparent ''fluidity'' of these submicron DPPC domains for BODIPY-DHPE and BODIPY-C12-DHPC must indicate a large degree of heterogeneity. Marked heterogeneities have been reported for unsupported bilayers that contain phase-separated domains (50) as well as for pure DPPC in both supported and unsupported bilayers (32). In the case here, formation of the gel domains could be disrupted by DOPC clusters surrounding the BODIPY-labeled phospholipid probes like surfactants (54). In the darkest regions of the larger domains (>1 μm), the DPPC appears to be more homogeneous (at least the phospholipid probes are being excluded to a larger extent), which explains why the mobility there is curtailed. Future studies should examine domain heterogeneity versus probe concentration and domain size.

If the phospholipid probes somehow disrupt the DPPC packing, the opposite may be true for the unmodified GM1 and Alexa-488 head-GM1. Given the preference of GM1 and Alexa-488 head-GM1 for the DPPC gel domains, they most likely do not disrupt the dense, ordered packing of the DPPC. Thus those DPPC domains containing Alexa-488 head-GM1, for example, may be more homogenous, rendering the probe immobile. Possible evidence for this notion is the observation in Fig. 4 that the boundary FCS curves data showed an immobile component that indicates uniform, tight DPPC packing up the domain boundary. Another factor concerning immobility in the DPPC domains for both Alexa-488 head-GM1 and BODIPY-C5-GM1 probes is that they may undergo significant clustering (46,55); however, we see no evidence of large-scale clustering in the AFM topography or fluorescence. In the next section, we show that the only evidence for clustering occurs due to CTX-B binding, which reduces mobility in the fluid DOPC phase.

Diffusion in liquid-disordered DOPC regions: binding of CTX-B to GM1

In this section, we examine effects of CTX-B binding on the mobility of the GM1 components in the DOPC fluid phase. First of all, we find that the location of the fluorophore has little or no effect on the diffusion of the free (unbound) BODIPY-C5-GM1 and Alexa-488 head-GM1 in DOPC, whereas we saw above (e.g., Fig. 2) that it has a large effect on partitioning between fluid and gel domains. When BODIPY-C5-GM1 is bound to B-CTX-B, the diffusion is slowed by at least a factor of six relative to the unbound BODIPY-C5-GM1 (see Fig. 8, *C* and *D*). Since the asialoganglioside-derived Alexa-488 head-GM1 cannot bind CTX-B (56), we instead

compare its diffusion to trace amounts of native GM1 in DOPC that are bound to Alexa-488-CTX-B (Fig. 3, *A* and *B*). Once again, we observe that the diffusion of the Alexa-488-CTX-B-bound GM1 is slower, by a similar factor, than the unbound Alexa-488 head-GM1. These results are consistent with the notion that CTX-B forms pentamers that may bind up to five GM1 molecules in a cluster (47). A large cluster, that probably includes DOPC matrix lipids as well, is expected to move at a slower rate. Similar mobility changes with clustering have been observed for peptides in vesicles (57). The data contrast sharply, however, with measurements recently reported (14) for Alexa-488-CTX-B-bound GM1 diffusion in vesicles that are comparable to unbound lipid probes (5×10^{-8} cm^2/s).

Of particular interest is the mobility data for BODIPY-C5-GM1 after binding to B-CTX-B. Since the latter is bound only to the accessible BODIPY-C5-GM1 in the distal leaflet, one may expect the unbound BODIPY-C5-GM1 in the proximal leaflet to remain fully mobile, resulting in a distinct fast/slow two-component fit for the two leaflets. However, this is not what we observe. We find no evidence for a fully mobile fast component ($D_{fast} > 10^{-8}$ cm^2/s). Thus it appears that a strong coupling between the two leaflets (33) somehow slows the mobility of the unbound proximal BODIPY-C5-GM1. One possibility is that interleaflet coupling may induce clustering of the proximal BODIPY-C5-GM1 in a mirror image of the B-CTX-B-bound BODIPY-C5-GM1 in the distal leaflet. An important conclusion, therefore, is that interleaflet coupling in this model membrane appears to be more dominant than substrate effects (33).

Diffusion in liquid-disordered DOPC regions: two-component fits for PC probes

The lateral diffusion coefficients of the GM1 and PC lipid probes in the liquid-disordered DOPC phase are averages derived from many (>10) FCS sets taken in each region determined by AFM topography to be free of DPPC domains. All the bound and unbound GM1 probes (headgroup-labeled, tailgroup-labeled, and native) have FCS autocorrelation curves that generally fit fairly well with a one-component (D) lateral diffusion model. Two-component fits (D_{fast} and D_{slow}) are always better, of course, but also have greater variability among the FCS curves (hence the larger SDs). Thus we have tabulated both sets of fits in Table 1. Surprisingly, the data also suggest no clear evidence of a slow component that would arise from a strong interaction of the large GM1 headgroup with the substrate.

However, the case is very different for BODIPY-DHPE and BODIPY-C12-DHPC data in DOPC. These probes always require a two-component fit in the lateral diffusion analysis. The difference can be seen in Fig. 9, where we show a representative FCS curve from BODIPY-DHPE (Fig. 9 *A*) that requires a two-component fit and a representative FCS curve from Alexa-488 head-GM1 (Fig. 9 *B*) that has a one-component fit. There are possible systematic artifacts that may lead to poor one-component fits (58,59), due primarily to inadequate control over optical parameters. In the case here, we have appropriately optimized those parameters (see Materials and Methods) and have exercised great care to maintain a constant laser intensity, spot size, and spatial filter throughout this work. Although artifacts certainly cannot be dismissed, the fact that we are seeing two-component ''effects'' dominating for one set of probes and not another dispels systematic error as the cause. Thus we attribute the persistent two-component lateral diffusion of the phospholipid probes to a physical origin such as substrate interactions (33,36), bilayer heterogeneities (11,32,50), or multiple orientations of the probe itself relative to the membrane surface (60,61).

The D_{fast} diffusion components in Table 1 for unbound lipid probes (2–4 $\times$ 10^{-8} cm^2/s) are comparable to those previously measured for phospholipid and cyanine probes in both supported (22,23,33) and unsupported bilayers (11,21). It is tempting to attribute the D_{slow} diffusion component (0.08–0.4 $\times$ 10^{-8} cm^2/s) to probes in the proximal leaflet that are pinned by the substrate. Separate FRAP diffusion measurements of lipid probes in the proximal and distal leaflets on glass-supported bilayers revealed no difference in mobility ((1.3 $\pm$ 0.2) $\times$ 10^{-8} cm^2/s (33), (3.6 $\pm$ 0.5) $\times$ 10^{-8} cm^2/s (22)). Immobile fractions of 10–20% in both leaflets were also reported. In NMR studies of silica-bead-supported

TABLE 1 Two-dimensional translational diffusion coefficients for labeled lipid probes in DOPC and DPPC

	DOPC domains				
	D*	D_{fast}*	D_{slow}*		DPPC domains
Lipid probe	(one-component fit)	(two-component fit)		C_{fast}/C_{slow}	D*
BODIPY-C5-GM1	1.4 ± 0.4	3.62 ± 0.77	0.29 ± 0.13	2.7 ± 1.1	<0.001
BODIPY-C5-GM1 bound to B-CTX-B	0.13 ± 0.04	0.68 ± 0.15	0.035 ± 0.008	0.97 ± 0.4	<0.001[†]
Alexa-488 head-GM1	1.20 ± 0.29	3.61 ± 0.72	0.40 ± 0.09	1.78 ± 0.6	<0.001
GM1, bound to Alexa-488 CTX-B	0.040 ± 0.011	0.50 ± 0.10	0.016 ± 0.007	0.54 ± 0.17	<0.001
BODIPY-DHPE	N/A	3.71 ± 0.71	0.16 ± 0.05	1.6 ± 0.4	>1.0[‡]
BODIPY-C12-DHPC	N/A	2.50 ± 0.78	0.076 ± 0.048	1.24 ± 0.3	>1.0[‡]

*($\times 10^{-8}$cm^2/s), ± SD.

[†]Variable, some evidence observed for higher mobilities in submicron domains.

[‡]Submicron DPPC domains; immobility observed for domains >1 μm.

DPPC bilayers (36), the proximal leaflet was more ordered and had half the mobility (7.5×10^{-8} cm^2/s, at 55°C) of the distal leaflet.

There are several reasons, however, that we cannot solely attribute the slow diffusion component to the presence of the substrate. If the slow component is due to a significant fraction (C_{fast}/C_{slow} varies from ~1.2 to 3 in Table 1) of lipids that are influenced by substrate interactions, it is difficult to understand why the interactions are significantly less pronounced for the GM1 probes that have a much larger headgroup that the PC probes. This observation also discounts a notion that slow probe mobilities are due to a greater viscosity of the proximal leaflet induced by substrate interactions and/or an ordered water layer between the bilayer and the substrate. Furthermore, a strong interleaflet coupling, as noted in the previous section, would be expected to transfer significant substrate effects across the bilayer thereby reducing mobility for both leaflets. Finally, long-range electrostatic interactions with negative charges on the glass substrate are not considered to be a factor because we used a fairly high ionic strength buffer (150 mM NaCl PBS) that effectively shields substrate charges (62). When that buffer was replaced with 15 mM NaCl PBS buffer, and later with distilled water, no changes in the FCS data were observed. Interestingly, large decreases in mobility for both tailgroup-labeled BODIPY-C12-DHPC and headgroup-labeled rhodamine-DHPE have been observed in stacked lipid multilayers where Na^+ was increased from 0 mM (~7×10^{-8} cm^2/s) to 110 mM Na^+ (~1.4×10^{-8} cm^2/s (63)). The reduced mobility was attributed to clusters of three or more lipids bound together by the Na^+.

Bilayer heterogeneities in the fluid DOPC phase are difficult to assess. One advantage of this work is that AFM topographic maps provide sufficient detail with <10 nm resolution to rule out significant defects and domains not observable with other methods. Since obstructions to diffusion are mapped out and avoided, we do not attempt to fit the FCS curves with a time-dependent anomalous diffusion coefficient $D \propto t^{\alpha - 1}$, where α varies from 0.7 to 1.0 depending on the obstacle concentration (30,64). Obvious heterogeneities due to domain boundaries are shown in Figs. 4 and 5. Subtle heterogeneities, however, due to local packing or tilting would not be easily detected by AFM and may not be considered an obstruction in the anomalous diffusion model. In any case, for BODIPY-DHPE and BODIPY-C12-DHPC, the two-component curves are not subject to much variability since they are consistently observed for all spots in all the bilayers tested.

Fluorescent labels have been blamed for affecting the mobility of bound proteins, although it was thought to be due to the increased size of the complex (65). In the case here, significant effects to mobility (and partitioning) could be caused by the tendency for the BODIPY moiety to seek specific depths in the bilayer (60). In their study of unsupported DOPC model membranes containing BODIPY headgroup- and tailgroup-labeled PC probes, Kaiser and London (60) were able to show that a significant population of the BODIPY groups, despite their nonpolarity, exhibits a tendency to be located near the polar region of the bilayer. The remaining BODIPY groups are buried in the hydrophobic depths of the bilayer. Clearly, for the tailgroup-labeled BODIPY-C12-DHPC, the BODIPY has to ''loop back toward the surface'' (60), creating a large perturbation in the local packing of the surrounding lipids. Similarly, for BODIPY-DHPE, the BODIPY loops back toward the bilayer to seek polar groups and/or hydrophobic depths. The local distortion in the bilayer for such occurrences could involve many matrix DOPC lipids and thus could cause a loss of mobility due to the increased ''free area'' required for motion (64,66). Furthermore, given this scenario of BODIPY-induced molecular distortion, it would be very easy to understand why the phospholipid probes tend to be excluded from the tightly packed DPPC domains or cause significant perturbations in the DPPC packing. These effects are expected to be less pronounced for BODIPY-C5-GM1 because of the closer proximity of the BODIPY label on the short acyl chain to the polar region of the bilayer. Although the rhodamine-like label on Alexa-488 head-GM1 may not distort the orientation of the bulky headgroup, this may also explain why it is not excluded from the DPPC gel domains. Many important questions remain, however, as to how much of an effect local distortion in lipid structure has on mobility. The roughly linear dependence of lateral diffusion strictly on surface free area (66) is fairly mild relative to the difference between D_{fast} and D_{slow} diffusion components measured here.

SUMMARY AND CONCLUSIONS

We have demonstrated that two-dimensional diffusion in supported model membranes can be characterized locally by instrumentation that provides simultaneous AFM and fluorescence imaging of lipid domains. The AFM images not only provide nm-scale lateral resolution and topographic information but are used to reveal domain partitioning on the submicron scale of four different fluorescence probes that are used to obtain mobilities. The four probes were chosen because they are fluorescent analogs of naturally occurring lipids and they represent two common labeling schemes requiring headgroup and tailgroup modification. Overall, we find that the supported model membranes examined here have common attributes in structure and fluidity with unsupported vesicles; however, we have also presented unexpected results that suggest possible fluorophore effects on probe partitioning, domain heterogeneity, and probe mobility.

Partitioning of lipid components into membrane domains is central to the lipid raft model. We see here that the exclusion of labeled probes by their unlabeled counterparts in gel domains is indicative of significant perturbations in packing and/or lipid interactions, consistent with previous studies on supported and unsupported model membranes.

For both saturated phospholipid analogs BODIPY-C12-DHPC and BODIPY-DHPE, we see that modifications in either the acyl chain or the headgroup lead to exclusion from the saturated gel domains. For the GM1 analogs, we find that BODIPY-C5-GM1 is excluded from the gel domains, whereas Alexa-488 head-GM1 is not excluded. Thus the presence of the fluorescent label on the asialoganglioside headgroup does not interfere with the interactions that allow GM1 to occupy sites in the gel-phase DPPC.

Equally important in the lipid raft model of membrane function is the mobility of the lipid components inside and outside domains. Overall, we found that the mobilities of all four probes were roughly the same in the DOPC fluid phase. Thus we found no glaring difference in fluid phase mobility due to the location of the head- or tailgroup labeling. Both BODIPY-C5-GM1 and unmodified GM1 were shown to slow down by at least a factor of six upon binding to CTX-B fragments, which most likely indicates clustering induced by the pentameric CTX-B. Mobility of the unbound GM1 analogs is severely attenuated in the gel-phase DPPC. This is definitely the case for the Alexa-488 head-GM1, indicating a tight packing by the surrounding DPPC lipids. Furthermore, mobility appears to be restricted around the domain boundaries. The mobility in DPPC is also restricted for BODIPY-C5-GM1; however, evidence was presented for increased mobility in submicron domains that may be due to DPPC packing heterogeneities. Mobility around the domain boundaries is higher, resembling, for the most part, that in the fluid phase. This trend of increasing mobility in and around the submicron DPPC domains is remarkably prevalent in the BODIPY-C12-DHPC and BODIPY-DHPE phospholipid analogs. For these probes there appears to be little reduction in the lateral diffusion in the submicron DPPC domains relative to the DOPC regions. It is important to point out that these unexpected observations for the phospholipid analogs are not general for all DPPC domain sizes (immobility was detected in the center of large domains) and that a comprehensive study on mobilities versus domain size was not performed. However, the results presented here for submicron domains may be relevant to mobility in sphingolipid-cholesterol domains in biological membranes, where domain sizes are believed to be <100 nm (3,67). Thus its appears that those lipids such as Alexa-488 head-GM1 and unmodified GM1 that partition into the DPPC domains do not disrupt the dense packing and thus are rendered immobile, whereas those lipids that are excluded on the basis of disrupting the gel packing and/or lipid-lipid interactions may have greater mobility.

In general, we have shown that FCS can reveal heterogeneities in supported lipid bilayers. The phospholipid probes BODIPY-C12-DHPC and BODIPY-DHPE not only exhibited a perplexing mobility in submicron DPPC domains but also required two-component fits to the FCS curves in the fluid DOPC phase. The slow component could be due to a variety of factors including substrate interactions and membrane heterogeneities. However, it could also be due to local distortion of the molecule and surrounding matrix lipids by the tendency of BODIPY to seek polar regions of the membrane. This effect, documented elsewhere (60), may also be responsible for exclusion of the probes from close-packed gel domains. In any case, it is clear that the phospholipid probes, as well as other labeled phospholipids using different fluorophores, are not ideal for the modeling of partitioning and mobility in membranes. They do, however, illustrate that lipid components and lipid-protein complexes in biological membranes could move rapidly in and out of raft domains as needed.

The authors thank Mark Stevens for critical comments. Molecular structure images were kindly provided by Avanti Polar Lipids.

This research was supported in part by the Division of Materials Science and Engineering, Office of Basic Energy Sciences, U.S. Department of Energy, and National Institutes of Health K25AI060036. Sandia is a multiprogram laboratory operated by Sandia, a Lockheed Martin company, for the U.S. Department of Energy under contract DE-AC04-94AL85000.

REFERENCES

1. Brown, D. A., and E. London. 1998. Functions of lipid rafts in biological membranes. *Annu. Rev. Cell Dev. Biol.* 14:111–136.
2. Simons, K., and E. Ikonen. 1997. Functional rafts in cell membranes. *Nature.* 387:569–572.
3. Edidin, M. 2003. The state of lipid rafts: from model membranes to cells. *Annu. Rev. Biophys. Biomol. Struct.* 32:257–283.
4. Varma, R., and S. Mayor. 1998. GPI-anchored proteins are organized in submicron domains at the cell surface. *Nature.* 394:798–801.
5. Pyenta, P., D. Holowka, and B. Baird. 2001. Cross-correlation analysis of inner-leaflet-anchored green fluorescent protein co-redistributed with IgE receptors and outer leaflet lipid raft components. *Biophys. J.* 80: 2120–2132.
6. Gaus, K., E. Gratton, E. Kable, A. Jones, I. Gelissen, L. Kritharides, and W. Jessup. 2003. Visualizing lipid structure and raft domains in living cells with two-photon microscopy. *Proc. Natl. Acad. Sci. USA.* 100:15554–15559.
7. Tang, Q., and M. Edidin. 2003. Lowering the barriers to random walks on the cell surface. *Biophys. J.* 84:400–407.
8. Kenworthy, A., B. Nichols, C. Remmert, G. Hendrix, M. Kumar, J. Zimmerberg, and J. Lippincott-Schwartz. 2004. Dynamics of putative raft-associated proteins at the cell surface. *J. Cell Biol.* 165: 735–746.
9. Dietrich, C., B. Yang, T. Fujiwara, A. Kusumi, and K. Jacobson. 2002. Relationship of lipid rafts to transient confinement zones detected by single particle tracking. *Biophys. J.* 82:274–284.
10. Murase, K., T. Fujiwara, Y. Umemura, K. Suzuki, R. Iino, H. Yamashita, M. Saito, H. Murakoshi, K. Ritchie, and A. Kusumi. 2004. Ultrafine membrane compartments for molecular diffusion as revealed by single molecule techniques. *Biophys. J.* 86:4075–4093.
11. Schwille, P., J. Korlach, and W. W. Webb. 1999. Fluorescence correlation spectroscopy with single-molecule sensitivity on cell and model membranes. *Cytometry.* 36:176–182.
12. Schwille, P. 2001. Fluorescence correlation spectroscopy and its potential for intracellular applications. *Cell Biochem. Biophys.* 34: 383–408.
13. Rigler, R., and E. Elson. 2001. Fluorescence Correlation Spectroscopy: Theory and Applications. F. Schäefer, J. Toennies, and W. Zinth, editors. Springer-Verlag, Berlin/Heidelberg.

14. Bacia, K., I. Majoul, and P. Schwille. 2002. Probing the endocytic pathway in live cells using dual-color fluorescence cross-correlation analysis. *Biophys. J.* 83:1184–1193.

15. Bacia, K., D. Scherfeld, N. Kahya, and P. Schwille. 2004. Fluorescence correlation spectroscopy relates rafts in model and native membranes. *Biophys. J.* 87:1034–1043.

16. Dietrich, C., L. A. Bagatolli, Z. N. Volovyk, N. L. Thompson, M. Levi, K. Jacobson, and E. Gratton. 2001. Lipid rafts reconstituted in model membranes. *Biophys. J.* 80:1417–1428.

17. Dietrich, C., Z. N. Volovyk, M. Levi, N. L. Thompson, and K. Jacobson. 2001. Partitioning of Thy-1, GM1, and cross-linked phospholipid analogs into lipid rafts reconstituted in supported model membrane monolayers. *Proc. Natl. Acad. Sci. USA.* 98:10642–10647.

18. Wang, T.-Y., and J. R. Silvius. 2000. Different sphingolipids show differential partitioning into sphingolipid/cholesterol-rich domains in lipid bilayers. *Biophys. J.* 79:1478–1489.

19. Wang, T.-Y., and J. R. Silvius. 2003. Sphingolipid partitioning into ordered domains in cholesterol-free and cholesterol-containing lipid bilayers. *Biophys. J.* 84:367–378.

20. Korlach, J., P. Schwille, W. W. Webb, and G. W. Feigenson. 1999. Characterization of lipid bilayer phases by confocal microscopy and fluorescence correlation spectroscopy. *Proc. Natl. Acad. Sci. USA.* 96:8461–8466.

21. Scherfeld, D., N. Kahya, and P. Schwille. 2003. Lipid dynamics and domain formation in model membranes composed of ternary mixtures of unsaturated and saturated phosphatidylcholines and cholesterol. *Biophys. J.* 85:3758–3768.

22. Kalb, E., S. Frey, and L. Tamm. 1992. Formation of supported planar bilayers by fusion of vesicles to supported phospholipid monolayers. *Biochim. Biophys. Acta.* 1103:307–316.

23. Ratto, T., and M. Longo. 2003. Anomalous subdiffusion in heterogeneous lipid bilayers. *Langmuir.* 19:1788–1793.

24. Schütz, G., H. Schindler, and T. Schmidt. 1997. Single-molecule microscopy on model membranes reveals anomalous diffusion. *Biophys. J.* 73:1073–1080.

25. Martin, D., M. Forstner, and J. Käs. 2002. Apparent subdiffusion inherent to single particle tracking. *Biophys. J.* 83:2109–2117.

26. Dufrêne, Y., W. Barger, J.-B. Green, and G. Lee. 1997. Nanometer-scale surface properties of mixed phospholipid monolayers and bilayers. *Langmuir.* 13:4779–4784.

27. Yuan, C., J. Furlong, P. Burgos, and L. J. Johnston. 2002. The size of lipid rafts: an atomic force microscopy study of ganglioside GM1 domains in sphingomyelin/DOPC/cholesterol membranes. *Biophys. J.* 82:2526–2535.

28. Burns, A. 2003. Domain structure in model membrane bilayers investigated by simultaneous atomic force microscopy and fluorescence imaging. *Langmuir.* 19:8358–8363.

29. Boxer, S. G. 2000. Molecular transport and organization in supported lipid membranes. *Curr. Opin. Chem. Biol.* 4:704–709.

30. Ratto, T., and M. Longo. 2002. Obstructed diffusion in phase-separated supported lipid bilayers: a combined atomic force microscopy and fluorescence recovery after photobleaching approach. *Biophys. J.* 83: 3380–3392.

31. Benda, A., M. Benes, V. Marecek, A. Lhotsky, W. Hermens, and M. Hof. 2003. How to determine diffusion coefficients in planar phospholipid systems by confocal fluorescence correlation spectroscopy. *Langmuir.* 19:4120–4126.

32. Stevens, B., and T. Ha. 2004. Discrete and heterogeneous rotational dynamics of single membrane probe dyes in gel phase supported bilayer. *J. Chem. Phys.* 120:3030–3038.

33. Merkel, R., E. Sackmann, and E. Evans. 1989. Molecular friction and epistatic coupling between monolayers in supported monolayers. *Journal de Physique France.* 50:1535–1555.

34. Johnson, S. J., T. M. Bayerl, D. C. McDermott, G. W. Adam, A. R. Rennie, R. K. Thomas, and E. Sackmann. 1991. Structure of an adsorbed dimyristoylphosphatidylcholine bilayer measured with specular reflection of neutrons. *Biophys. J.* 59:289–294.

35. Sackmann, E. 1996. Supported membranes: scientific and practical applications. *Science.* 271:43–48.

36. Hetzer, M., S. Heinz, S. Grage, and T. Bayerl. 1998. Asymmetric molecular friction in supported phospholipid bilayers revealed by NMR measurements of lipid diffusion. *Langmuir.* 14:982–984.

37. Stottrup, B., S. Veatch, and S. Keller. 2004. Nonequilibrium behavior in supported lipid membranes containing cholesterol. *Biophys. J.* 86: 2942–2950.

38. Leonenko, Z., E. Finot, H. Ma, T. Dahms, and D. Cramb. 2004. Investigation of temperature-induced phase transitions in DOPC and DPPC phospholipid bilayers using temperature-controlled scanning force microscopy. *Biophys. J.* 86:3783–3793.

39. Xie, A., R. Yamada, A. Gewirth, and S. Granick. 2002. Materials science of the gel to fluid phase transition in a supported phospholipid bilayer. *Phys. Rev. Lett.* 89:246103.

40. O'Shannessy, D. 1990. Antibodies biotinylated via sugar moieties. *In* Avidin-Biotin Technology. M. Wilchek and A. Bayer, editors. Academic Press, London. 163.

41. Sheppard, C., and D. Shotton. 1997. Confocal Laser Scanning Microscopy. Springer-Verlag, New York.

42. Rigler, R., U. Mets, J. Widengren, and P. Kask. 1993. Fluorescence correlation spectroscopy with high count rate and low background: analysis of translational diffusion. *Eur. Biophys. J.* 22:169–175.

43. Hues, S., C. Draper, K. Lee, and R. Colton. 1994. Effect of PZT and PMN actuator hysteresis and creep on nanoindentation measurements using force microscopy. *Rev. Sci. Instrum.* 65:1561–1565.

44. Widengren, J., U. Mets, and R. Rigler. 1995. Fluorescence correlation spectroscopy of triplet states in solution: a theoretical and experimental study. *J. Phys. Chem.* 99:13368–13379.

45. Radhakrishnan, A., T. G. Anderson, and H. M. McConnell. 2000. Condensed complexes, rafts, and the chemical activity of cholesterol in membranes. *Proc. Natl. Acad. Sci. USA.* 97:12422–12427.

46. Yuan, C., and L. J. Johnston. 2001. Atomic force microscopy studies of ganglioside GM1 domains in phosphatidylcholine and phosphatidylcholine/cholesterol bilayers. *Biophys. J.* 81:1059–1069.

47. Miller, C., J. Majewski, R. Faller, S. Satija, and T. Kuhl. 2004. Cholera toxin assault on lipid monolayers containing ganglioside GM_1. *Biophys. J.* 86:3700–3708.

48. Burgos, P., C. Yuan, M. Viriot, and L. Johnston. 2003. Two-color near-field fluorescence microscopy studies of microdomains (''rafts'') in model membranes. *Langmuir.* 19:8002–8009.

49. Bagatolli, L. A., and E. Gratton. 2000. A correlation between lipid domain shape and binary phospholipid mixture composition in free standing bilayers: a two-photon fluorescence microscopy study. *Biophys. J.* 79:434–447.

50. Silvius, J. R. 2003. Fluorescence energy transfer reveals microdomain formation at physiological temperatures in lipid mixtures modeling the outer leaflet of the plasma membrane. *Biophys. J.* 85:1034–1045.

51. Bagatolli, L. A., and E. Gratton. 2000. Two photon fluorescence microscopy of coexisting lipid domains in giant unilamellar vesicles of binary phospholipid mixtures. *Biophys. J.* 78:290–305.

52. Veatch, S. L., and S. L. Keller. 2002. Organization in lipid membranes containing cholesterol. *Phys. Rev. Lett.* 89:268101.

53. Giocondi, M.-C., V. Vié, E. Lesniewska, P.-E. Milhiet, M. Zinke-Allmang, and C. Le Grimellec. 2001. Phase topology and growth of single domains in lipid bilayers. *Langmuir.* 17:1653–1659.

54. de Almeida, R., L. Loura, A. Fedorov, and M. Prieto. 2002. Nonequilibrium phenomena in the separation of a two-component lipid bilayer. *Biophys. J.* 82:823–834.

55. Milhiet, P.-E., V. Vié, M.-C. Giocondi, and C. Le Grimellec. 2001. AFM characterization of model rafts in supported bilayers. *Single Molecule.* 2:109–112.

56. MacKenzie, C., T. Hirama, K. Lee, E. Altman, and N. Young. 1997. Quantitative analysis of bacterial toxin affinity and specificity for glycolipid receptors by surface plasmon resonance. *J. Biol. Chem.* 272: 5533–5538.

57. Lee, C., and N. Petersen. 2003. The lateral diffusion coefficient of selectively aggregated peptides in giant unilamellar vesicles. *Biophys. J.* 84:1756–1764.

58. Hess, S., and W. Webb. 2002. Focal volume optics and experimental artifacts in confocal fluorescence correlation spectroscopy. *Biophys. J.* 83:2300–2317.

59. Enderlein, J., I. Gregor, D. Patra, and J. Fitter. 2004. Art and artifacts of fluorescence correlation spectroscopy. *Curr. Pharm. Biotechnol.* 5: 155–161.

60. Kaiser, R., and E. London. 1998. Determination of the depth of BODIPY probes in model membranes by parallax analysis of fluorescence quenching. *Biochim. Biophys. Acta.* 1375:13–22.

61. Klymchenko, A., G. Duportail, A. Demchenko, and Y. Mély. 2004. Bimodal distribution and fluorescence response of environment-sensitive probes in lipid bilayers. *Biophys. J.* 86:2929–2941.

62. Müller, D. J., D. Fotiadis, S. Scheuring, S. Müller, and A. Engel. 1999. Electrostatically balanced subnanometer imaging of biological specimens by atomic force microscope. *Biophys. J.* 76:1101–1111.

63. Böckmann, R., A. Hac, T. Heimburg, and H. Grubmüller. 2003. Effect of sodium chloride on a lipid bilayer. *Biophys. J.* 85:1647–1655.

64. Saxton, M. 1999. Lateral diffusion of lipids and proteins. *In* Current Topics in Membranes. D. Deamer, A. Kleinzeller, and D. Fambrough, editors. Academic Press, New York. 229–282.

65. Zhang, F., W. Schmidt, Y. Hou, A. Williams, and K. Jacobson. 1992. Spontaneous incorporation of the glycosyl-phophatidylinositol-linked protein Thy-1 into cell membranes. *Proc. Natl. Acad. Sci. USA.* 89: 5231–5235.

66. Liu, C., A. Paprica, and N. Peterson. 1997. Effects of size of macrocyclic polyamides on their rate of diffusion in model membranes. *Biophys. J.* 73:2580–2587.

67. Simons, K., and W. Vaz. 2004. Model membranes, lipid rafts, and cell membranes. *Annu. Rev. Biophys. Biomol. Struct.* 33:269–295.